Effect of Texture and Grain Size on Bio-Corrosion Response of Ultrafine-Grained Titanium

N.P. GURAO, GEETHA MANIVASAGAM, P. GOVINDARAJ, R. ASOKAMANI, and SATYAM SUWAS

The bio-corrosion response of ultrafine-grained commercially pure titanium processed by different routes of equal-channel angular pressing has been studied in simulated body fluid. The results indicate that the samples processed through route B_c that involved rotation of the workpiece by 90 deg in the same sense between each pass exhibited higher corrosion resistance compared to the ones processed by other routes of equal-channel angular pressing, as well as the coarse-grained sample. For a similar grain size, the higher corrosion resistance of the samples exhibiting off-basal texture compared to shear texture indicates the major role of texture in corrosion behavior. It is postulated that an optimum combination of microstructure and crystallographic texture can lead to high strength and excellent corrosion resistance.

I. INTRODUCTION

FOR the past few decades, commercially pure titanium (CP-Ti) and titanium-based alloys have been used extensively for biomedical applications due to their excellent corrosion resistance, low modulus, superior biocompatibility, and osseointegration behavior in comparison to conventional biomedical alloys, such as type 316 stainless steel and cobalt chromium alloys.[1–3] The biocompatibility and corrosion resistance of titanium are the result of a passive TiO_2 film of thickness 2 to 6 nm formed on the titanium surface.[4] Titanium alloy Ti-6Al-4V is a well-studied material for orthopedic applications; however, the leaching of Al and V in due course of time results in toxicity and neurological disorders.[1] It has been noticed that the corrosion at the head-neck taper of the femoral component in metal on metal implants has led to severe corrosion and the leached ions have resulted in adverse tissue reactions.[5] Apart from corrosion, the failure of the Ti-6Al-4V implant due to poor fatigue strength, low wear resistance, high modulus of elasticity, and lack of osseointegration has also been clinically observed.[6–8] Thus, it is very essential to choose alloying elements that will reduce the modulus of elasticity, enhance the hardness of the alloy, and minimize the toxic effects of the leached ions.

An alternative option is to use unalloyed titanium with high strength and superior corrosion resistance. In order to improve the surface hardness and corrosion resistance of the unalloyed titanium, surface modification techniques like anodic oxidation treatment,[9] electrochemical treatment,[10] sandblasting,[11] carbide coatings,[12] laser nitriding,[13] electrolytic polishing,[14] etc., have been carried out. Recently, severe plastic deformation-based techniques have also been envisaged to improve the mechanical properties of titanium.

Severe plastic deformation (SPD)-based processes lead to an ultrafine grain size ($d \sim 100$ to 1000 nm) in metallic materials contributing to superior grain size strengthening compared to conventional microcrystalline materials.[15,16] Enhancement in strength and reduction in modulus were observed for warm-rolled ultrafine-grained Ti-13Nb-13Zr alloy.[17] In addition, various SPD techniques like equal-channel angular pressing (ECAP), accumulative roll bonding (ARB), multi-axial forging (MAF), and high pressure torsion (HPT) have been developed for producing ultrafine grain size materials. Among these techniques, ECAP is by far the most well studied and widely used SPD technique till date. The ECAP-processed materials have great potential for usage in various structural as well as biomedical applications. It has been clearly demonstrated that there is a considerable increase in hardness, fatigue strength, and yield strength and a moderate decrease in modulus of elasticity of CP-Ti processed through different ECAP routes compared to Ti-6Al-4V.[18,19] This special attribute renders it a far superior material to be used for load-bearing biomedical applications as it does not contain any non-bio-compatible alloying additions which are present in the currently used biomedical alloy Ti-6Al-4V.[1]

N.P GURAO, formerly Ph.D. Student with the Department of Materials Engineering, Indian Institute of Science, Bangalore 560012, India, is now Assistant Professor with the Indian Institute of Technology, Kanpur, India. GEETHA MANIVASAGAM, Professor, is with the School of Mechanical and Building Sciences (SMBS), VIT University, Vellore 632014, India. Contact e-mail: gmv1225@yahoo.com P. GOVINDARAJ, formerly Student with the School of Bio Sciences and Technology (SBST), VIT University, Vellore 632014, India, is now Assistant Professor with Alpha College of Engineering, Thirumazhisai, Chennai, India. R. ASOKAMANI, Professor, formerly with the School of Mechanical and Building Sciences (SMBS), VIT University, is now with the Dhanalakshmi College of Engineering, Dr. VPR Nagar, Thambaram, Chennai 601301, India. SATYAM SUWAS, Associate Professor, is with the Department of Materials Engineering, Indian Institute of Science.

The work carried out by Thorpe et al.[20] has clearly demonstrated that UFG Ti exhibits enhanced corrosion resistance compared to coarse-grained (CG) polycrystalline titanium. Balyanov et al.[21] found that UFG Ti produced by ECAP had better corrosion resistance than CG Ti in both HCl and H_2SO_4 solutions. Recent studies of Balakrishnan et al.[22] also revealed that UFG-Ti produced by ECAP exhibited superior corrosion behavior compared to coarse-grained CP-Ti in simulated body fluid solution.

In addition to grain size, grain boundary character, and hardness, the corrosion response of the ECAP-processed material is also dependent on crystallographic texture.[20–22] It is, however, difficult to isolate the effects of microstructure and texture for a given ECAP sample. The only way to address this issue is to extract the samples from the same billet along different orientations. Moreover, the samples processed through different routes up to the same strain level may also lead to different textures, but similar microstructures. In the present investigation, we aim to deconvolute the effect of grain size and texture on the corrosion behavior of CP-Ti processed by ECAP. The corrosion behavior of the ultrafine-grained (UFG) CP-Ti processed by different routes of ECAP is compared with the starting material in Hank's solution (simulated body fluid) which was maintained at 37 ± 1 °C. The contribution of texture and microstructural refinement to the corrosion resistance of CP-Ti is explored in the present investigation.

II. MATERIALS AND METHODS

A. Processing

The CP-Ti samples were processed employing ECAP in a specially designed die[23] with an inter-channel angle of 90 deg. ECAP was carried out at 673 K (400 °C) following three different routes namely route A, B_c, and C on billets with dimensions 10 mm × 10 mm × 100 mm at a crosshead speed of 0.1 mm/s. In route A, the sample is pressed repetitively without rotation around the extrusion axis, while in route B_C the sample is rotated by 90 deg between each pass, whereas in route C the sample is rotated by 180 deg between successive passes. A schematic diagram showing different ECAP routes is shown in Figure 1(a). The samples processed through routes A and C were subjected to 3 ECAP passes, while the samples processed through route B_c were deformed to 4 passes. The details of processing have been discussed elsewhere by one of the present authors.[24]

B. Characterization of Microstructure and Texture

The microstructures of the materials before and after ECAP processing were characterized by optical microscopy (OM), scanning electron microscopy-based electron back scatter diffraction (SEM-EBSD), and transmission electron microscopy (TEM). Microstructural observations were made on both the cross-sectional (ND-TD) plane of the billet and on the
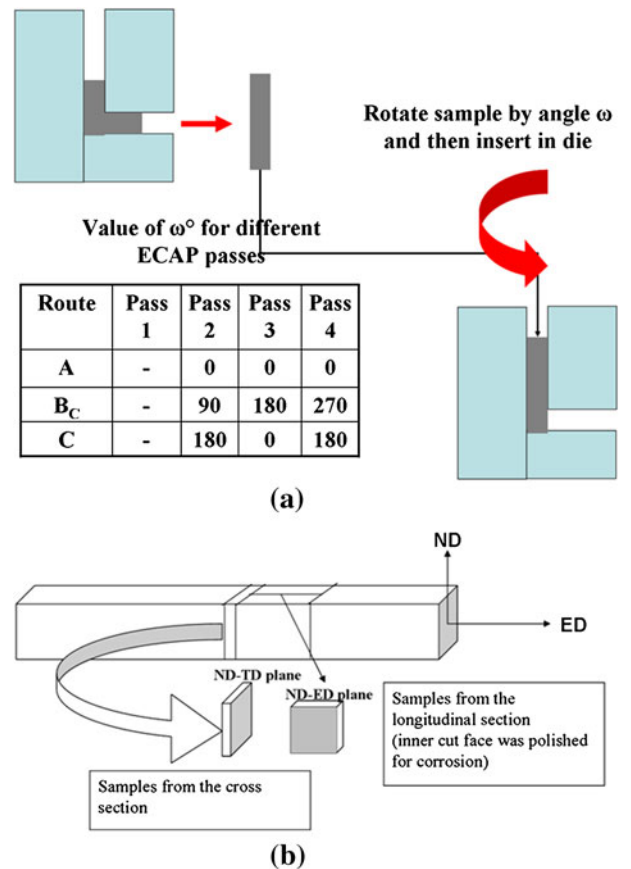

Fig. 1—(a) Schematic showing processing of a billet using different ECAP passes and (b) Cross section and longitudinal section of the ECAP-processed sample.

transverse (ND-ED) plane. Texture measurements were carried out by the X-ray diffraction method (Co K_α radiation, $\lambda = 1.790$ Å) following Schulz reflection geometry. A set of six incomplete pole figures, namely, $(10\bar{1}0)$, (0002), $(10\bar{1}1)$, $(10\bar{1}2)$, $(11\bar{2}0)$, and $(11\bar{2}2)$, was recorded for all the samples. Texture data was generated for the ED plane (cross section) as well as for the TD plane of the billets (Figure 1(b)). Specimens selected from each category were examined using a scanning electron microscope (SEM) attached with EBSD detector. The EBSD data analysis was carried out using the TSL software (Tex SEM Laboratory, version 5.2). TEM was carried out using a JEOL 2000 FX transmission electron microscope operating at 200 kV.

Vickers hardness was measured on a Zwick system with a load of 50 g. Five measurements were carried out at the mid thickness of the ECAP samples on the lateral and longitudinal planes to avoid any frictional effects and obtain statistically meaningful data.

C. Electrochemical Measurements

Electrochemical measurements were performed on samples extracted from both lateral (ED) and longitudinal (TD) planes (Figure 1(b)). For the corrosion tests, square-shaped specimens with an area of 100 mm² and

Table I. CG and ECAP CP-Ti Samples Process Conditions

S. No.	Sample Description	Pass Conditions	Deformed Temperature [K (°C)]
1	CG CP-Ti	—	—
2	A1 (route A)	1 pass	673 (400)
3	A2 (route A)	2 pass	673 (400)
4	A3 (route A)	3 pass	673 (400)
5	B2 (route B_c)	2 pass	673 (400)
6	B3 (route B_c)	3 pass	673 (400)
7	B4 (route B_c)	4 pass	673 (400)
8	C2 (route C)	2 pass	673 (400)
9	C3 (route C)	3 pass	673 (400)

5 mm in thickness were used. The details of the samples used for corrosion studies are given in Table I. Prior to the electro-chemical measurement, the specimens were mechanically polished up to 1200 grit SiC paper. Then, the specimens were rinsed with distilled water and ultrasonically cleaned in acetone to remove the impurities from the surface.

The bio-corrosion tests were performed in simulated body fluid condition using Hank's solution. Freshly prepared Hank's solution comprising NaCl, NaHCO$_3$, MgCl$_2$·6H$_2$O, MgSO$_4$·7H$_2$O, KH$_2$PO$_4$, KCl, CaCl$_2$, Na$_2$HPO$_4$, and D(+) glucose (C$_6$H$_{12}$O$_6$) dissolved in distilled water and buffered at 310 K (37 °C) at pH of 7.4 was used for corrosion tests.

The corrosion potential and polarization curves were obtained using a potentiostat. The electrochemical cell consisting of a three-electrode setup with working electrode, a reference electrode (RE), a saturated standard calomel electrode (SCE), and a platinum foil as counter electrode or auxiliary electrode (AE), was used in the present investigation. This setup was connected to a potentiostat (Gill AC Version 5, ACM instruments, UK) and operated through a computer. The experimental materials (CG and UFG samples), after polishing, were wrapped with Teflon and 6-mm-diameter window from the surface of the samples was exposed to the solution. Prior to the electrochemical measurement, the open-circuit potential (OCP) *vs* time measurements were carried out to obtain the corrosion response of the specimens under equilibrium conditions for 30 minutes in the simulated body environment. The samples were immersed in Hank's solution for 60 minutes to attain a steady open-circuit potential, which was measured as the corrosion potential. When the specimen attained a constant potential, the potentiodynamic polarization was started from an initial potential of 250 mV below the corrosion potential (E_{corr}). The scan rate of 0.166 mV/s was used and the current density *vs* potential was plotted. The polarization tests were repeated thrice for each specimen to insure the reproducibility of the results. For determining the corrosion current, the Tafel extrapolation method was used and the Tafel plots were obtained in the range of +100 to −100 mV with respect to the rest potential (E_{corr}). The intersection of the lines gives the I_{corr} value. The corrosion rate was then determined using the following equation[25,26]:

$$\text{Corrosion rate} = I_{corr} * K * EW/dA,$$

where EW represents equivalent weight (g/equivalent), d refers to density in g/cm^3, and A is the area in cm^2.

III. RESULTS AND DISCUSSION

A. *Microstructure*

The optical micrographs of the coarse-grained (CG) starting material and the ultrafine-grained (UFG) ECAP samples are shown in Figures 2 and 3 on the ND-ED and ND-TD planes, respectively. Microstructural features indicate that the deformation is quite heterogeneous throughout the process. In general, elongated structures can be seen around many grains that originate from accommodation strains of the neighboring grains. The macroscopic shear in the intersection plane of the channels elongates the grains in specific directions; one can identify a general orientation of the elongated grain boundaries. The inclination angles of these "stringers" are in good agreement with the theoretically expected orientations with respect to the ED direction.[25] Figure 3 represents the microstructure corresponding to the ED plane where the deformation features although apparent have a different geometry from that on the TD plane. The stringers visible on the TD plane are not seen on the ED plane and the grain shapes appear almost equiaxed. The gradual refinement of the grains with the increase in number of passes is clearly seen in Figure 3.

Figure 4 shows the EBSD measurements of the microstructures of the samples obtained after ECAP with low and high angle grain boundaries superimposed on a blank map. In each case, the microstructure is quite heterogeneous showing refined grains as well as the grains that are not fragmented, but having small orientation gradients. Within these grains, the misorientation does not exceed 5 deg. They are inclined at a particular angle with respect to ED. The heterogeneity tends to disappear after the third pass where the fraction of fine grains became reasonably high. In the fourth pass of the route B_c-processed material, the microstructure appears equiaxed and shows lower grain orientation spread, thereby indicating a recrystallized microstructure. The microstructures were further analyzed by TEM Figure 5 shows bright field TEM micrographs after three ECAP passes for all the three routes A, B_c, and C and for the 4-pass route B_c sample. A clear evolution of substructure is observed in all the cases. The features indicate a large deformation followed by some recovery in the material. In addition, deformation twins (marked T) are observed in the sample processed by route A. The route B_c sample which was subjected to four passes shows clear evidence of recrystallization (marked R).

B. *Crystallographic Texture*

The experimental texture of the undeformed coarse-grained material is presented in terms of the (0002) pole
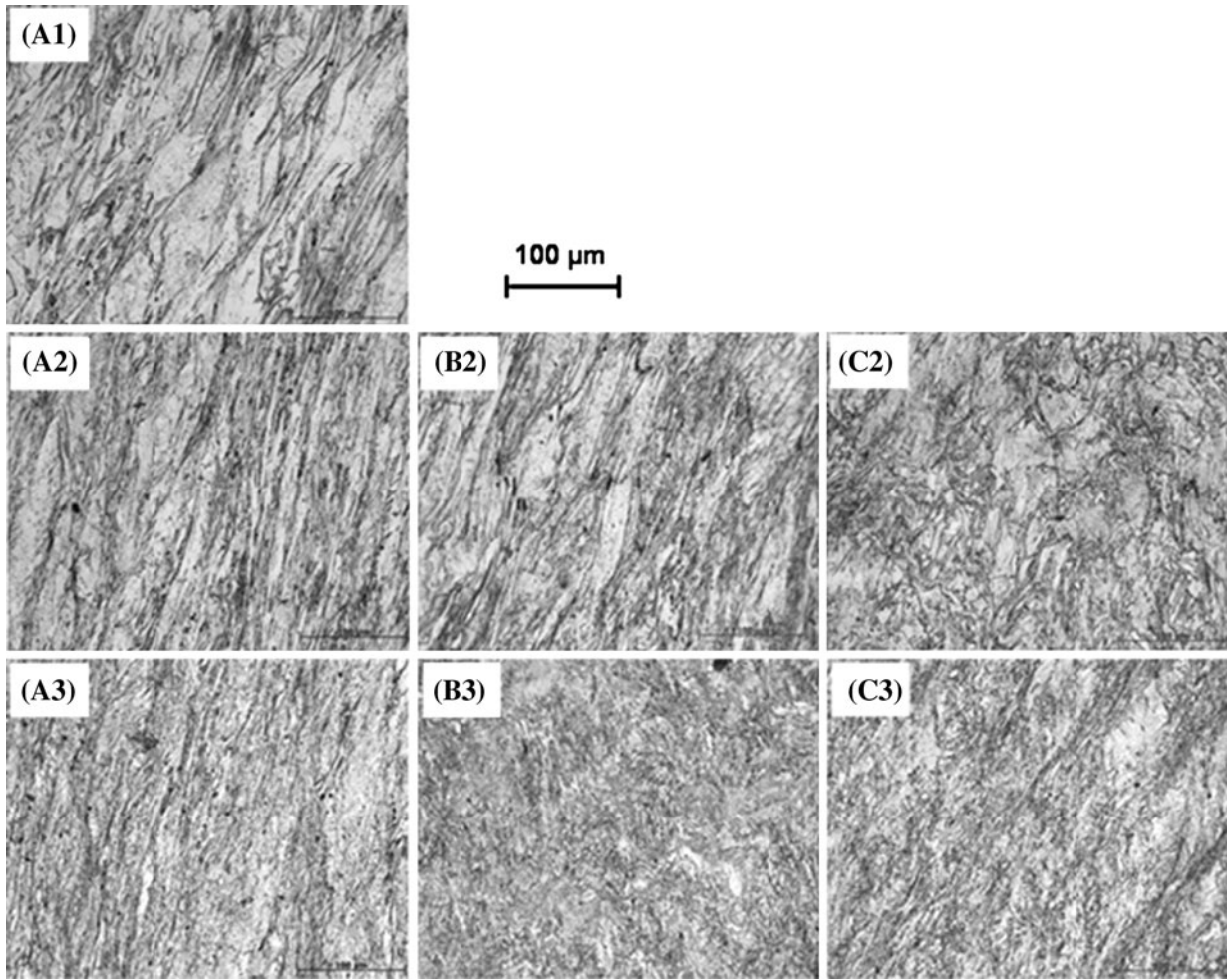
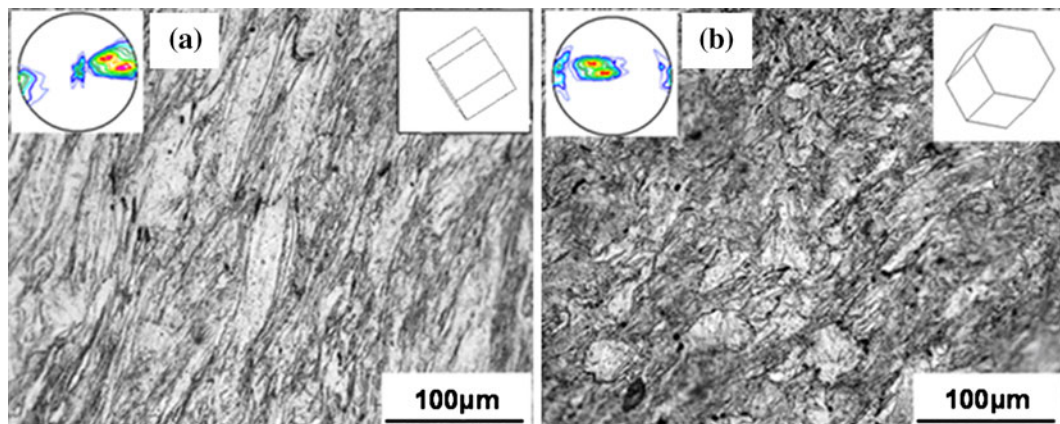Fig. 2—Optical micrographs on the TD plane of the ECAP samples.

Fig. 3—Optical micrographs on the (*a*) TD and (*b*) ED plane of the ECAE B2 sample. The TD plane shows elongated grains and stringers, while the ED plane shows equiaxed grains. The inset shows the orientation of the HCP unit cell of titanium in most of the grains of the deformed samples.

figures, obtained for the normal (ND) and transverse (TD) plane in Figure 6(a). The (0002) pole figures of ECAP deformed fine-grained materials are presented in

Figures 6(b) and (c) on the TD and ED projection planes, respectively. The pole figure of the starting material displays the split TD texture with a significant spread of
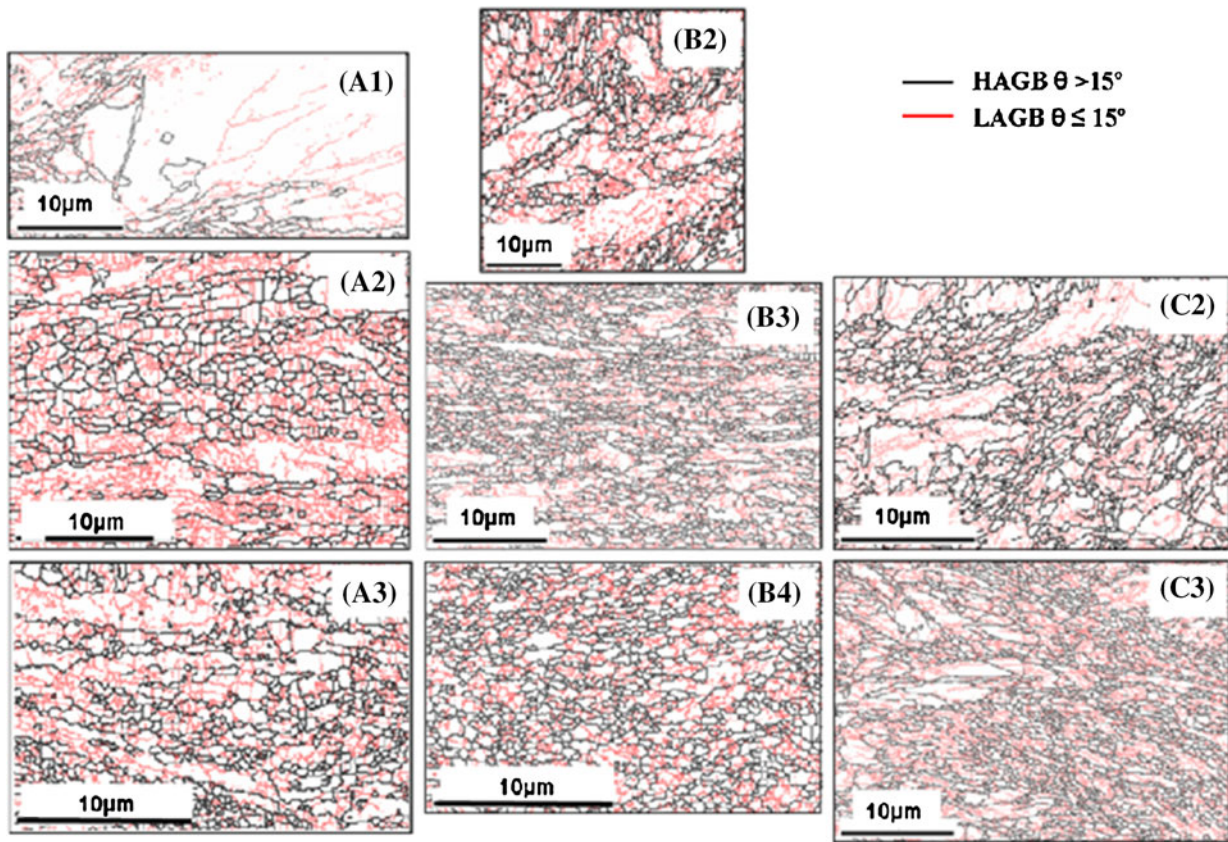
Fig. 4—Grain boundary maps showing high angle grain boundaries ($\theta > 15$ deg) and low angle grain boundaries ($\theta < 15$ deg) of the ECAP samples obtained from EBSD.
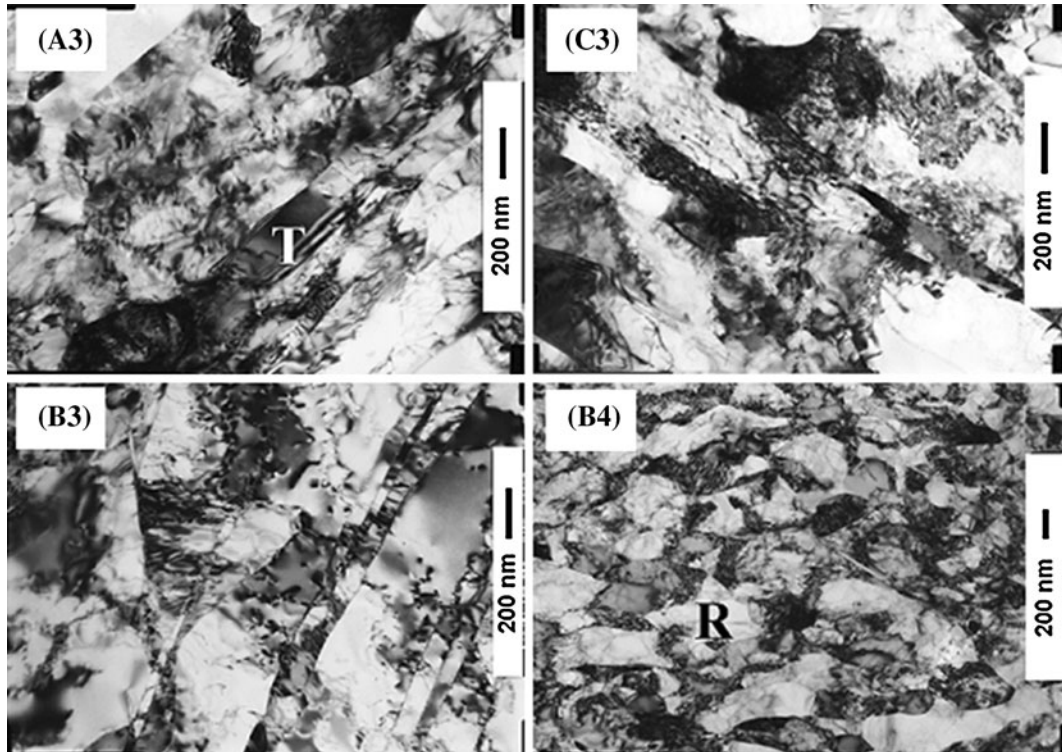

Fig. 5—Transmission electron microscopy images for the ECAP samples deformed to 3 passes with different routes. The microstructures are characterized by heavily deformed regions (black), recovered and recrystallized grains (R) and twins (T).
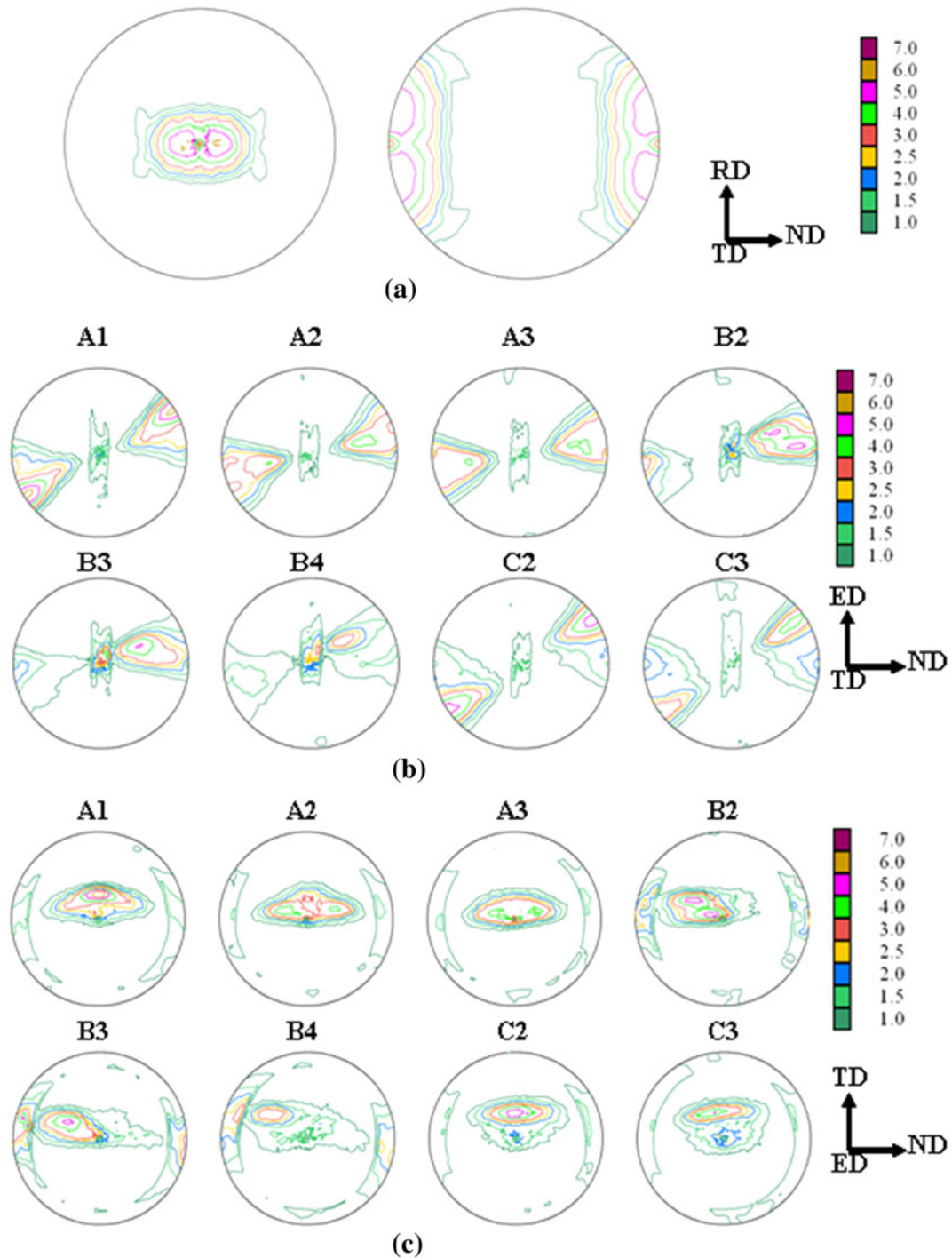
Fig. 6—(a) Recalculated (0002) pole figure from the starting material on ED and TD plane, (b) Recalculated (0002) pole figure from the experimental data on the TD plane showing shear texture, (c) (0002) pole figure from the experimental data on the ED plane showing off-basal texture.

about 20 to 30 deg along ND and ED directions. For the ECAP-processed materials, the pole figures clearly show a shear-type texture on the TD plane.[23,27] On the other hand, the ED plane shows the clustering of basal poles at an off-basal orientation toward the ND. The textures of the ECAP-processed material obtained by different routes may appear similar at first sight; however, there are subtle differences. The texture remains the same with

the number of passes for the route A-processed material. The texture reversal occurs, however imperfectly, for route C and route B_c. A similar texture evolves only after 4 passes for route B_c. Nevertheless, the TD plane is characterized by the clustering of basal poles at 90 deg away from the TD in between the ED and ND directions. This is a rotated shear texture commonly seen in ECAP of hexagonal metals and alloys.[24,27]

C. Corrosion Potentials

Figure 7 represents the open-circuit potential *vs* time for samples processed by ECAP (UFG-Ti) and CG CP-Ti. In the present study, E_{corr} for the ECAP-processed CP-Ti was lesser than that of undeformed CG CP-Ti indicating that coarse-grained CP-Ti possesses a strong passive layer which is more noble than the layer formed on the UFG sample. However, on exposing to simulated body fluid, the potential measured did not vary much with time for the UFG sample indicating that the oxide formed on the surface of the UFG is highly stable with time. The magnitude of E_{corr} that depends on the composition of the metal, environment, and reactions at the electrode is not the only parameter that allows characterization of the corrosion phenomenon in a given system. In general, a metal with lower (negative) potential is prone to more corrosion. However, there is a possibility that when inhibition of the cathodic reaction takes place due to quicker passivation, this potential may acquire more negative values.

D. Polarization Curves

The corrosion response of the samples subjected to potentiodynamic studies is presented in Figures 8 and 9. Figure 8 shows the potentiodynamic plots for CG and ECAP-deformed UFG samples in simulated body fluid solution at 37 ± 1 °C. These curves show qualitatively similar behavior, but with different values of their electrochemical data for the CG and UFG material. The potentiodynamic plots for CP-Ti processed by different routes (Route A, B_c, and C) up to three passes are shown in Figure 9, while the comparison among the corrosion behaviors of samples cut along the ED and TD planes is presented in Figure 10. Among all the samples, the sample processed through route B_c exhibited lower i_{corr} and increased corrosion resistance values (Table II). This clearly demonstrates that corrosion rates are significantly lower for ECAP-processed samples compared to the coarse-grained material in simulated body fluid solution. Table III shows the electrochemical properties of UFG samples cut along
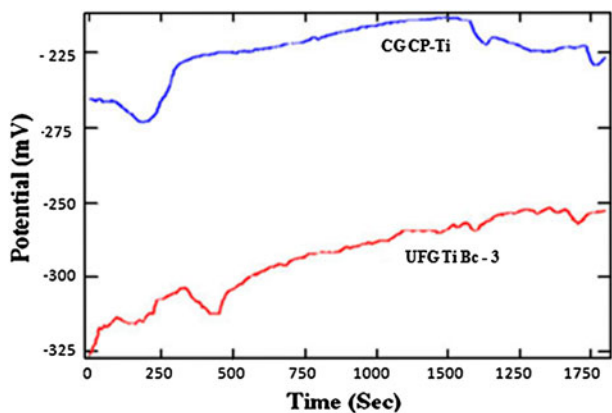
the TD for the routes A, B_c, and C. It was observed that the corrosion current (i_{corr}) and corrosion rate (mpy) of the UFG material were much lower (~1/7 times) than that of CG CP-Ti. The results of the present investigation corroborate the finding of Balyanov *et al.*[21] who demonstrated that the samples subjected to 8 passes (B_c)
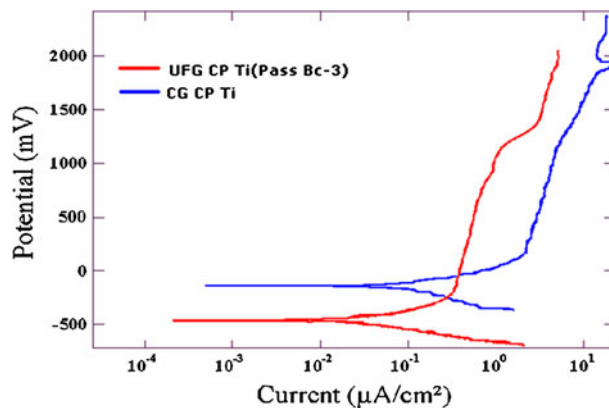
Fig. 8—Potentiodynamic plots of CG and UFG CP-Ti (3 passes).

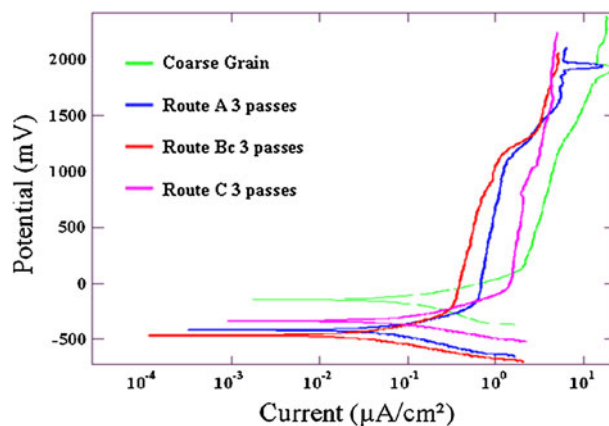Fig. 9—Potentiodynamic plots of CG and ED plane UFG CP-Ti route A, B_c, and C (3 passes).
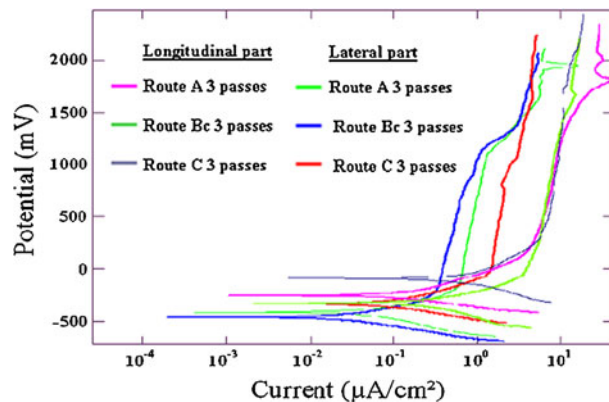
Fig. 7—Open-circuit potentials of CG and UFG CP-Ti in simulated body fluid solution.

Fig. 10—Potentiodynamic plots of ED plane and TD plane UFG CP-Ti route A, B_c, and C.

Table II. Electrochemical Properties of CG and UFG CP-Ti (ED Plane) in Simulated Body Fluid Solution

S. No.	Sample Description	Micro Hardness (HV) Load (0.490 N)	Texture Index	I_{corr} ($\mu A/cm^2$)	E_{corr} (mV)	Corrosion Rate Mils Per Year (mm/year)
1	CG CP Ti	184	**	0.726	−216	0.00629
2	673 K (400 °C) 1 pass	207	2.912	0.187	−415	0.00160
3	A2 (route A)	216	2.883	0.472	−363	0.00408
4	A3 (route A)	225	3.023	0.248	−410	0.00213
5	B2 (route B_c)	238	3.899	0.260	−390	0.00226
6	B3 (route B_c)	242	4.097	0.098	−461	0.00083
7	B4 (route B_c)	238	1.733	0.260	−355	0.00223
8	C2 (route C)	222	2.226	0.304	−362	0.00261
9	C3 (route C)	227	2.023	0.635	−335	0.00551

**not valid as the texture is qualitatively different from ECAP material.

Table III. Electrochemical Properties of CG and UFG CP-Ti (TD Plane) in Simulated Body Fluid Solution

S. No.	Sample Description	Average Grain Size (nm)	Micro Hardness (Vickers Hardness) HV	I_{corr} ($\mu A/cm^2$)	E_{corr} (mV)	Corrosion Rate Mils Per Year (mm/year)
1	A3 (route A)	658	245	1.193	−260	0.0104
2	B3 (route B_c)	708	248	1.315	−318	0.0114
3	B4 (route B_c)	680	265	0.641	−256	0.0056
4	C3 (route C)	711	245	2.908	−97	0.0253

with the smallest grain size exhibited the highest corrosion resistance.

E. Effect of Crystallographic Texture on Corrosion

It is understood that apart from grain size, crystallographic texture and grain boundary character distribution also play an important role in determining the corrosion response of a material. A general observation is that there is a decrease in corrosion rate with an increase in the texture strength. In order to have a better quantification of texture, the texture index was calculated from the corresponding orientation distribution functions.[24,27] It is, however, difficult to find an exact correlation between the texture index (as well as grain size) on corrosion rate because such a simplified assumption does not account for boundaries with special character, like the twin boundary. The corrosion rate is rather a complex function of grain size, orientation, and grain boundary character. However, it can be safely concluded that there is an inverse relationship between texture index and corrosion rate.

It is evident that the samples cut along the TD plane exhibit higher corrosion compared to the ED plane (Tables II and III). The lower corrosion resistance of the samples cut along the TD plane in spite of their high hardness value can be attributed to the difference in the crystallographic texture between the TD and the ED samples. Hoseini et al.[17] have proposed that the basal planes in hexagonal titanium are the closely packed planes and hence are resistant to corrosion and oxidation attack compared to the {10$\bar{1}$0} and {11$\bar{2}$0} planes. They further argued that in addition to the grain size, texture is a dominant parameter in determining the corrosion response of SPD-processed titanium. In the present investigation, maximum corrosion resistance is observed for the off-basal texture on the ED plane compared to the shear texture on the TD plane. Hoseini et al.[17] also observed maximum corrosion resistance for ECAP 2-pass B_c sample with off-basal texture on the ED plane. The higher corrosion rate on the TD plane of the ECAP samples than that of the CG material could be attributed to the drastic difference in the texture of the starting material with basal texture compared to the TD plane of ECAP samples. It can be concluded that texture also plays an important role in determining the corrosion response of titanium in addition to grain size. A direct correlation between the texture index and the corrosion resistance is a clear indication for the same. It can be seen that off-basal texture leads to better corrosion resistance. Therefore, a processing technique that leads to off-basal texture with ultrafine grain sizes can lead to high strength and even better corrosion resistance.

IV. CONCLUSIONS

A detailed investigation on the corrosion behavior of CP-Ti processed *via* all the three important routes of ECAP in simulated body fluid was carried out to deconvolute the effect of microstructure and texture on corrosion behavior of HCP titanium. The major findings of this study are summarized below.

1. The UFG Ti produced by ECAP shows better corrosion resistance than CG Ti in simulated body fluid. The corrosion potential E_{corr} for the UFG-Ti was more negative than that of coarse-grained CP-Ti. Among different processed ECAP samples,

the 3-pass route B$_c$ sample with minimum grain size exhibits the highest corrosion resistance. This can be attributed to the formation of highly stable oxide film on metal surface with higher grain boundary fraction.

2. There is a significant difference in the corrosion response at the TD and ED planes of the as-received as well as the ECAP-processed samples. This result clearly indicates that crystallographic texture has a major role in determining the corrosion behavior of the anisotropic hexagonal close-packed titanium, though grain size and hardness also influence the corrosion behavior.

3. By suitably designing the processing route, the synergistic relation between microstructure and crystallographic texture can be explored to produce high strength materials with superior corrosion resistance.

REFERENCES

1. M. Geetha, A.K. Singh, A.K. Gogia, and R. Asokamani: *Prog. Mater Sci.*, 2009, vol. 54, pp. 397–425.
2. L.R. Rubin: *Biomaterials in Reconstructive Surgery*, C. V. Mosby Co., St. Louis, MO, 1983, pp. 158–228.
3. M. Esposito, J. Lausmaa, J.M. Hirsch, and P. Thomsen: *J. Biomed. Mater. Res.*, 1999, vol. 48, pp. 559–68.
4. D. Velten, V. Biehl, F. Aubertin, B. Valeske, W. Possart, and J. Breme: *J. Biomed. Mater. Res.*, 2002, vol. 59, pp. 18–28.
5. M. Long and H.J. Rack: *Biomaterials*, 1998, vol. 19, pp. 1621–39.
6. M. Niinomi: *J. Mech. Behav. Biomed. Mater.*, 2008, vol. 1, pp. 30–42.
7. G. Samuel: *Steinemann Periodontol*, 2000, vol. 17, pp. 7–21.
8. H.-J. Bunge: *Texture Analysis in Materials Science: Mathematical Methods*, Butterworth-Heinemann, London, 1983.
9. H.J. Song, M.K. Kim, G. Chun Jung, M. Sook Vang, and Y. Joon Park: *Surf. Coat. Technol.*, 2007, vol. 201, pp. 8738–45.
10. M. Masmoudi, M. Assoul, M. Wery, R. Abdelhedi, F. El Halouani, and G. Monteil: *Appl. Surf. Sci.*, 2006, vol. 253, pp. 2237–43.
11. X.P. Jiang, X.Y. Wang, J.X. Li, D.Y. Li, C.S. Man, M.J. Shepard, and T. Zhai: *Mater. Sci. Eng. A*, 2006, vol. 429, pp. 30–35.
12. L. He, X. Zhang, and C. Tong: *Surf. Coat. Technol.*, 2006, vol. 200, pp. 3016–20.
13. E. Carpene, M. Shinn, and P. Schaaf: *Appl. Surf. Sci.*, 2005, vol. 247, pp. 307–12.
14. A.S. Guilherme, G.E.P. Henriques, R.A. Zavanelli, and M.F. Mesquita: *J. Prosthet. Dent.*, 2005, vol. 93, pp. 378–85.
15. R.Z. Valiev, R.K. Islamgaliev, and I.V. Alexandrov: *Prog. Mater Sci.*, 2000, vol. 45, pp. 103–89.
16. K.S. Suresh, M. Geetha, C. Richard, J. Landoulsi, H. Ramasawmy, S. Suwas, and R. Asokamani: *Mater. Sci. Eng. C*, 2012, vol. 32, pp. 763–71.
17. M. Hoseini, A. Shahryari, S. Omanovic, and J.A. Szpunar: *Corros. Sci.*, 2009, vol. 51, pp. 3064–67.
18. H.J. Rack and J.I. Qazi: *Mater. Sci. Eng. C*, 2006, vol. 26, pp. 1269–77.
19. M. Greger, R. Kocich, and B. Kuretova: *Acta Metall. Sol.*, 2007, vol. 13, pp. 561–69.
20. S.J. Thorpe, B. Ramaswami, and A.T. Aust: *J. Electrochem. Soc.*, 1988, vol. 135, pp. 2162–70.
21. A. Balyanov, J. Kutnyakova, N.A. Amirkhanova, VV. Stolyarov, R.Z. Valiev, X.Z. Liao, Y.H. Zhao, Y.B. Jiang, H.F. Xu, T.C. Lowe, and Y.T. Zhu: *Scripta Mater.*, 2004, vol. 51, pp. 225–29.
22. A. Balakrishnan, B.C. Lee, T.N. Kim, and B.B. Panigrahi: *Biomater. Artif. Cells Artif. Organs*, 2008, vol. 22, pp. 1–7.
23. J.P. Mathieu, S. Suwas, L.S. Toth, A. Eberhardt, and P. Moll: *J. Mater. Proc. Technol.*, 2006, vol. 173, pp. 29–33.
24. S. Suwas, B. Beausir, L.S. Tóth, J.-J. Fundenberger, and G. Gottstein: *Acta Mater.*, 2011, vol. 59, pp. 1121–33.
25. Y.H. Zhao, Y.B. Jiang, H.F. Xu, T.C. Lowe, and Y.T. Zhu: *Scripta Mater.*, 2004, vol. 51, pp. 225–29.
26. D.A. Jones: *Principles and Prevention of Corrosion*, Macmillan, New York, 1992.
27. S. Suwas, L.S. Tóth, J.-J. Fundenburger, A. Eberhardt, and W. Skrotzki: *Scripta Mater.*, 2003, vol. 49, pp. 1203–08.